INTERNATIONAL JOURNAL FOR NUMERICAL METHODS IN FLUIDS
Int. J. Numer. Meth. Fluids **28**: 1073–1091 (1998)

ANALYSIS OF 3D BACKWARD-FACING STEP INCOMPRESSIBLE FLOWS VIA A LOCAL AVERAGE-BASED NUMERICAL PROCEDURE

G. DE STEFANO, F.M. DENARO* AND G. RICCARDI
Dipartimento di Ingegneria Aerospaziale, Seconda Università di Napoli, Aversa (Ce), Italy

SUMMARY

The study of the flow over a three-dimensional backward-facing step still provides interesting research when a new numerical method is developed and an investigation of the flow topology is performed. From a numerical point of view, accurate solutions are required, preferably with little computational effort, and the numerical results must lead to the understanding of the main features of the flow. The guidelines of an integrated framework are presented in this paper, starting with the description of the numerical methods for solving three-dimensional incompressible flows, based on a local-average procedure, up to the investigation of the flow structure by means of vortex lines reconstruction and vortices identification. Several results are reported concerning an analytical benchmark, simulation of flows in laminar and incipient transitional regimes and detection of vortical structures. Preliminary results for highly unsteady flows are also presented. © 1998 John Wiley & Sons, Ltd.

KEY WORDS: three-dimensional backward-facing step incompressible flow; local average procedure; multidimensional fluxes reconstruction; vortex lines; vortices identification

1. INTRODUCTION

The backward-facing step (BFS) flow in a channel has been extensively studied both numerically (e.g. [1–6]) and experimentally (e.g. [7,8]) during the last two decades. Despite its simple geometry, flow over the BFS shows some features of more complex geometry flows (i.e. separation, recirculation, reattachment), depending on Reynolds number (*Re*) and some geometrical parameters. Due to this fact, and also because the results of the numerical computations can be usefully compared with experimental data, it represents a good test case for any new numerical methodology. The flow regime can be varied by maintaining relatively moderate Reynolds numbers, ranging from laminar to fully developed turbulent flow. 3D numerical simulations are required, as the experiments of Armaly *et al*. [8] revealed that 2D flow conditions are only a particular case of a more general and complex situation. This fact can justify the lack of accordance between experimental and 2D numerical simulations, starting from $Re \cong 600$ (based upon the mean inlet velocity, defined as $\bar{U} = 2/3U_{\max}$, and the full channel height H). However, the appearance of a recovered two-dimensionality at $Re > 6000$, although it is only in an average meaning, justified some authors to perform 2D simulations of turbulent flows with and without turbulence modelling (e.g. [2,4,5]).

---

* Correspondence to: Dipartimento di Ingegneria Aerospaziale, Seconda Università di Napoli, via Roma, 29, 81031 Aversa (Ce), Italy.

CCC 0271–2091/98/171073–22$17.50

Received January 1997
Revised June 1997

This well-established picture was used as a basis for some fluid dynamics analysis studies, rather than numerical studies. In fact, stability, statistical and topological studies are applied to the results provided by numerical simulations based on several methodologies [3–5]. Currently, this has resulted in research, especially at high *Re* numbers. The present paper considers several steps: (i) a development of a methodology to integrate the Navier–Stokes equations in an accurate way, by considering that the generation of 'via via' smaller scales at higher Reynolds numbers cannot be described by resorting to a mesh refinement alone; (ii) an assessment of the influence of numerical boundary conditions[1]; (iii) a development of investigation tools in order to analyse vortical structures and to follow their motion. Each one of these issues results in source of dedicated researches. Herein, steps (i–iii) are dealt with by developing a global methodology to investigate three-dimensional unsteady flows. The present paper, although not exhaustive of all issues, addresses the reported guidelines.

The paper is organised as follows. A description of the numerical approach is given in Section 2: it generalises a previously reported approach [9,10] to three-dimensional incompressible Navier–Stokes equations. The main generalisation consists of a fully three-dimensional primitive variables formulation in average form and in the development of the projection equation, as an elliptic equation for an average-based pressure variable. This procedure is assessed in Section 3 via an accuracy order study based on a 3D analytical solution. Some results concerning laminar and incipient transitional regime, obtained from the application of different inlet conditions, are presented in Section 4. The analysis of the vorticity field is developed in Section 5, and a methodology is presented for the investigation of the three-dimensional behaviour of the flow. The application of standard techniques to detect vortical structures into BFS flows is discussed in Section 6. Finally, a preliminary analysis of a high Reynolds number flow is presented and some of the most relevant lines along which our investigation is currently developing are drawn in Section 7.

2. LOCAL AVERAGE-BASED PROCEDURE

The solution of the non-dimensional incompressible Navier–Stokes equations deals with the system of equations constituted by the momentum equation

$$\frac{\partial \mathbf{v}}{\partial t} + \underline{\nabla} \cdot \mathbf{v}\mathbf{v} + \underline{\nabla} p = \frac{1}{Re} \nabla^2 \mathbf{v}, \tag{1}$$

in a domain D, associated with the constraint

$$\underline{\nabla} \cdot \mathbf{v} = 0, \tag{2}$$

and with proper conditions assigned on the boundaries of the computational domain. For the domain considered here, the main geometrical parameters are the aspect ratio W/H, the expansion ratio $H/(H-S)$, where S is the step height and W is the spanwise length (see Figure 1, where the primary reattachment length x_r is also sketched). In all the presented results, the step height is fixed at $S = 0.5H$.

The velocity field $\mathbf{v}$, averaged on a control volume (CV) $\Omega(\mathbf{x}) \subset D$, is obtained at any time according to the following balance equation, written for the jth velocity component:

---

[1] This point in particular must be considered if a comparison of numerical with experimental results is required.

$$\bar{v}_j(\mathbf{x}, t^{n+1}) - \bar{v}_j(\mathbf{x}, t^n) = \frac{1}{|\Omega|}\int_{t^n}^{t^{n+1}} \mathrm{d}t \int_{\partial\Omega} \mathbf{n}\cdot\mathbf{f}_j \,\mathrm{d}S, \tag{3}$$

where the flux function $\mathbf{f}_j$ is expressed by

$$\mathbf{f}_j = -\mathbf{v}v_j - \mathbf{e}_j p + \frac{1}{Re}\underline{\nabla} v_j, \tag{4}$$

where $\mathbf{e}_j$ is the unit vector along the x_j-direction. The indices $j = 1, 2, 3$ refer to the streamwise (x), vertical (y) and spanwise (z) directions respectively, as shown in Figure 1. In each CV the jth average velocity component is defined as

$$\bar{v}_j(\mathbf{x}, t) = \frac{1}{|\Omega|}\int_{\Omega} v_j(\mathbf{x}', t)\,\mathrm{d}V(\mathbf{x}'). \tag{5}$$

The following subsections describe the adopted methodology. They present all of the fundamental steps for the extension of the local average direct numerical simulation (LADNS), reported in Reference [10], for 3D incompressible flows.

2.1. *A space-average based reconstruction for the flux function*

According to Equation (3), a functional relation is required to link the continuous flux function $\mathbf{f}_j$ to the set of averaged variables in the domain D. A natural choice is a Taylor expansion truncated to mth-order for the right-hand-side (RHS) of Equation (5), from which one obtains:

$$\bar{v}_j(\mathbf{x}, t) \cong \sum_{l=0}^{m} \frac{1}{l!}\frac{1}{|\Omega|}\int_{\Omega} [(x_r - x'_r)\partial_{x'_r}|_{\mathbf{x}}]^{(l)} v_j(\mathbf{x}', t)\,\mathrm{d}V(\mathbf{x}'), \tag{6}$$

having adopted index notation and the exponent in parentheses indicating a symbolic power. In this way the left-hand-side (LHS) of Equation (3) can be rewritten as

$$\Delta_t \bar{v}_j \equiv \bar{v}_j(\mathbf{x}, t^{n+1}) - \bar{v}_j(\mathbf{x}, t^n) \cong (I - R_s^{(m)})\Delta_t v_j, \tag{7}$$

where I is the identity operator at the point $\mathbf{x}$. This relation means that in each cell the local velocity component will be reconstructed [10] using the operator of mth accuracy order $R_s^{(m)}$, defined as

$$R_s^{(m)} g = -\sum_{l=1}^{m} \frac{1}{l!}\frac{1}{|\Omega|}\int_{\Omega} [(x_r - x'_r)\partial_{x'_r}|_{\mathbf{x}}]^{(l)} g(\mathbf{x}')\,\mathrm{d}V(\mathbf{x}'). \tag{8}$$

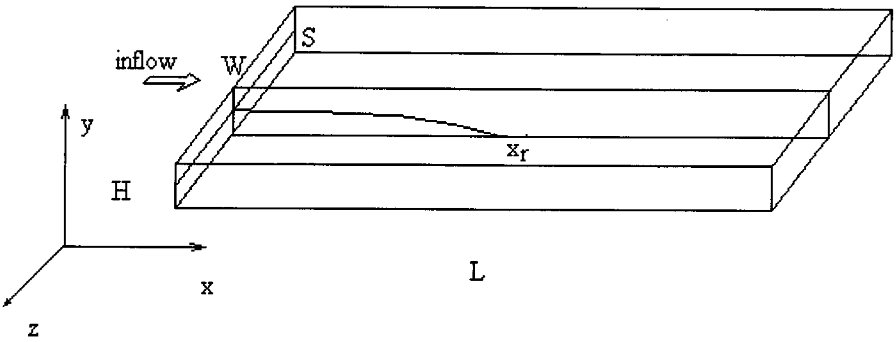

Figure 1. Sketch of the backward-facing step flow geometry. H, height of the channel; L, length; W, width; S, step height; x_r, primary reattachment length.

In the next subsection the treatment of RHS in Equation (3) is considered, by presenting the time integration procedure.

2.2. Time integration of the flux function

The time integration procedure consists of a step where the velocity component is updated according to Equation (3), by disregarding the pressure contribution in Equation (4). This is a basic fractional step and it can be related to the classical method of Chorin [11] and its successive formulations (e.g. [1,12]).

For each velocity component, a Taylor time expansion truncated to kth order is adopted, in which derivatives are replaced by the means of those of the momentum equation[2]. Thus, the time integral can be evaluated by introducing the integration operator of kth accuracy order $E_t^{(k)}$, which is reported for the sake of clarity (see also References [9,10]):

$$E_t^{(k)} \equiv I + \frac{\Delta t}{2} L_{\mathrm{ad}} + \cdots + \frac{\Delta t^{k-1}}{k!} L_{\mathrm{ad}}^{(k-1)}. \tag{9}$$

$L_{\mathrm{ad}} g = -\underline{\nabla} \cdot [\mathbf{v} g]$ defines the advective operator applied to a generic transported variable g. In this way, by choosing a suitable $k = k_1$, an evolutionary equation for an intermediate velocity field $\mathbf{v}^*$ can be written as

$$\begin{aligned}(I - R_s^{(m)}) v_j^*(\mathbf{x}', t^{n+1}) = (I - R_s^{(m)}) v_j(\mathbf{x}', t^n) &- \frac{\Delta t}{|\Omega|} \int_{\partial\Omega} \mathbf{n} \cdot \mathbf{v} E_t^{(k_1)} v_j(\mathbf{x}', t^n)\, \mathrm{d}S(\mathbf{x}') \\ &+ \frac{\Delta t}{|\Omega|} \int_{\partial\Omega} \mathbf{n} \cdot E_t^{(k_1)} \frac{1}{Re} \underline{\nabla} v_j(\mathbf{x}', t^n)\, \mathrm{d}S(\mathbf{x}'). \end{aligned} \tag{10}$$

This field has the property of providing the correct vorticity field (from a numerical point of view, correct is defined as the most accurate), without strictly respecting the constraint (2). Equation (10) has the form of a system of equations for the unknown velocity component $v_j^*(\mathbf{x}, t^{n+1})$. An implicit procedure can be used in order to solve it, but in this case, an alternative methodology is preferred:

$$v_j^*(\mathbf{x}', t^{n+1}) - v_j(\mathbf{x}', t^n) = \Delta t\, \partial_t v_j^*(\mathbf{x}', t)\big|_{t^n} + \cdots + O(\Delta t^{k_2}). \tag{11}$$

By successive derivations of Equation (1) (disregarding the pressure gradient), that are replaced in Equation (11) integrated over Ω, the system (10) can be expressed directly in diagonal form[3], as

$$\begin{aligned} & v_j^*(\mathbf{x}, t^{n+1}) - v_j(\mathbf{x}, t^n) \\ &= -\frac{\Delta t}{|\Omega|} \int_{\partial\Omega} \mathbf{n} \cdot [\mathbf{v} E_t^{(k_1)} + R_s^{(m)} \mathbf{v} E_t^{(k_2)}] v_j(\mathbf{x}', t^n)\, \mathrm{d}S(\mathbf{x}') \\ &\quad + \frac{\Delta t}{|\Omega|} \int_{\partial\Omega} \mathbf{n} \cdot [E_t^{(k_1)} + R_s^{(m)} E_t^{(k_2)}] \frac{1}{Re} \underline{\nabla} v_j(\mathbf{x}', t^n)\, \mathrm{d}S(\mathbf{x}'), \end{aligned} \tag{12}$$

where the advective and diffusive fluxes appear to be modified, to take the reconstruction procedure into account. Note that it is assumed that $\Omega(\mathbf{x}) = \mathbf{x} + \Omega(\mathbf{0})$ in Equation (12), so that spatial derivatives commute with integration.

---

[2] Higher order time derivatives of the momentum equation require a suitable linearisation of the advective flux, unless a slightly more complex procedure, involving a prediction of $\partial_t v_j$ and a subsequent correction, is used.

[3] Formally, the system (10) can also be inverted by considering that $(I - R_s^{(m)})^{-1} = I + R_s^{(m)} + (R_s^{(m)})^{(2)} + \cdots$, where the expansion results truncated to the mth power of a linear size of the CV.

2.3. The projection step: the averaged pressure equation

In order to ensure the final divergence-free velocity field, the pressure contribution must be taken into account. An equation for the time average pressure:

$$\langle p \rangle(\mathbf{x}') = \frac{1}{\Delta t}\int_{t^n}^{t^{n+1}} p(\mathbf{x}', t)\,\mathrm{d}t, \tag{13}$$

is herein obtained by taking the x_j derivative of both sides of Equation (3), summing over j and considering Equation (7), where the velocity field $\mathbf{v}(\mathbf{x}, t^{n+1})$ is imposed to be divergence-free:

$$\nabla^2 \tilde{p} = \frac{1}{\Delta t}\underline{\nabla}\cdot[\mathbf{v}^*(\mathbf{x}, t^{n+1}) - \mathbf{v}(\mathbf{x}, t^n)], \tag{14}$$

where a time-space averaged pressure field has been defined as

$$\tilde{p} \equiv \overline{(I + R_s^{(m)})\langle p \rangle}. \tag{15}$$

Therefore, Equation (14) results in a Poisson equation for the unknown pressure variable $\tilde{p}$, the gradient of which will correct the velocity field (12) in order to enforce the continuity.

In principle, Navier–Stokes equations do not require pressure boundary conditions, however, when the pressure equation is solved, it is necessary to assign some functional relation on the boundaries. No primitive pressure equation exists for iso-thermal incompressible fluids, as it is the pressure derived only from Equation (1) with the divergence-constraint. In the present approach, the equation for $\tilde{p}$ is associated to Neumann boundary conditions on ∂D, such that

$$\int_{\partial D} \frac{\partial \tilde{p}}{\partial n}\,\mathrm{d}S = \frac{1}{\Delta t}\int_{\partial D} [\mathbf{v}^*(\mathbf{x}, t^{n+1}) - \mathbf{v}(\mathbf{x}, t^n)]\cdot\mathbf{n}\,\mathrm{d}S. \tag{16}$$

The intermediate velocity field $\mathbf{v}^*$ is projected onto the space of divergence-free vector fields. Eventually, the single step time marching formula can be written as

$$\mathbf{v}(\mathbf{x}, t^{n+1}) = \mathbf{v}^*(\mathbf{x}, t^{n+1}) - \Delta t\underline{\nabla}\tilde{p}, \tag{17}$$

where $\mathbf{v}^*$ is given by Equation (12).

Finally, note that the present methodology, formulated in terms of integral balances, is suitable for application on both structured and unstructured grids. In the following section, the derived numerical scheme for 3D structured grids is presented.

3. NUMERICAL PROCEDURE AND STUDY OF THE ACCURACY ORDER

The computational domain is discretized by a structured grid of constant mesh size along each direction. This choice is justified by the fact that if a stretching along some direction was adopted, the result would be that $\partial\Omega$ is no longer space-independent and additional terms must be considered in Equation (12). Indeed, owing to its differential character, the reconstruction operator $R_s^{(m)}$ will also act on the space dependent boundary integral extremes. This would result in a heavy computational effort and the analyses of further accuracy problems are beyond the aims of the present paper[4].

---

[4] This matter has been recently studied by Ghosal and Moin [21], who developed the appropriate equations for stretched grids.

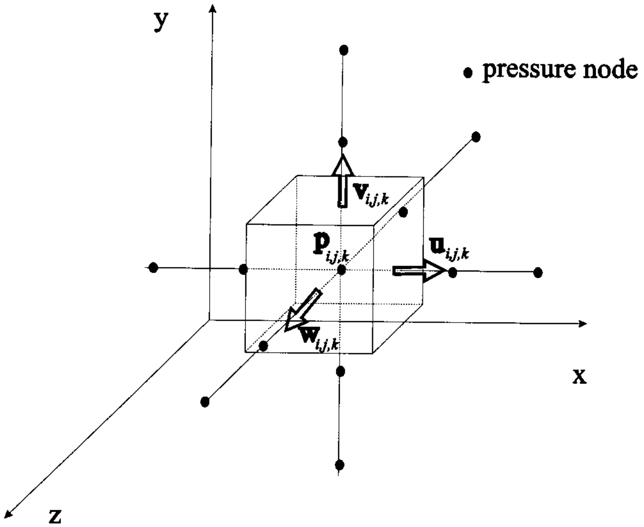

Figure 2. Control volume for the mass balance equation and sketch of the adopted staggering definition.

In order to impose the divergence-free constraint as accurately as possible, the variables are collocated on a staggered grid, as can be seen in Figure 2. The differential operators (Equations (8) and (9)), acting in Equation (12), are analytically applied by adopting a multidimensional second degree polynomial for each velocity component and a linear approximation for $\mathbf{n} \cdot \mathbf{v}$. The second degree polynomial is obtained by adopting a tetrahedron (Lagrangian simplex) as support region. This region is upwinded in the space following the velocity field, as shown in Figure 3. Such a fully three-dimensional criterion adopts a region among eight possible simplexes for each section. A new aspect worth noting in the present scheme is that the diffusive fluxes result computed on a flow-dependent stencil, and therefore, correctly considers the coupling between advection and diffusion during time

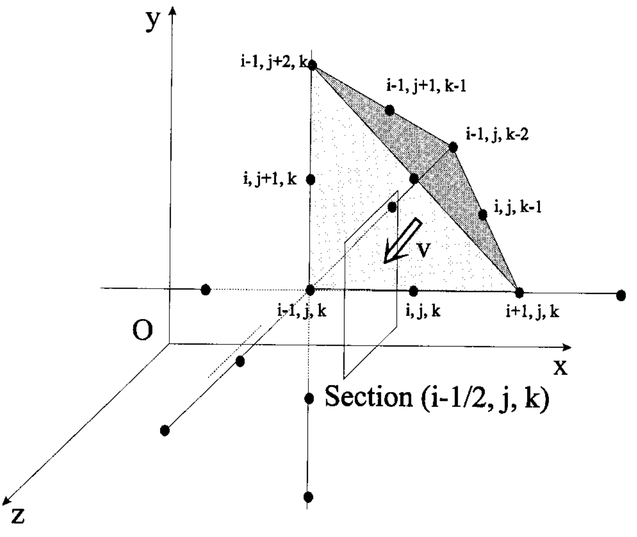

Figure 3. Example of three-dimensional upwind criterion applied to the section $(i-1/2, j, k)$ for $u<0$, $v<0$, $w>0$.

integration. According to the polynomial degree, we have fixed $k_1 = 3$, $m = 2$ and $k_2 = 1$ for the operators (Equations (8) and (9)). Finally, an integration over the boundaries has been performed analytically, leading to the discrete equation for the jth component on the (i, j, k) node:

$$(v_j^{*n+1})_{i,j,k} = (v_j^n)_{i,j,k} + \sum_{s=1}^{N \text{ sections}} F_s, \tag{18}$$

with $F_s = F_s^{(\mathrm{ad})} + F_s^{(\mathrm{dif})}$. For example, for the section s corresponding to $(i - 1/2, j, k)$, the result for the advective flux is

$$\begin{aligned} F^{(\mathrm{ad})}_{i-1/2,\,j,k} &= \frac{\Delta t}{|\Omega|} \int_{y-\Delta y/2}^{y+\Delta y/2} \mathrm{d}y' \int_{z-\Delta z/2}^{z+\Delta z/2} \mathrm{d}z' \mathbf{n} \cdot [\mathbf{v}E_t^{(3)} + R_s^{(2)}\mathbf{v}E_t^{(1)}] v_j(x - \Delta x/2, y', z', t^n) \\ &= c_x \left[C_1 + C_2(1 + c_x)\frac{\Delta x}{2} + C_3 c_y \frac{\Delta y}{2} + C_4 c_z \frac{\Delta z}{2} + C_5\, \Delta x\, \Delta y \left(\frac{c_x c_y}{3} + \frac{c_y}{4} \right) \right. \\ &\quad + C_6\, \Delta x\, \Delta z \left(\frac{c_x c_z}{3} + \frac{c_z}{4} \right) + C_7\, \Delta y\, \Delta z\, \frac{c_y c_z}{3} + C_8(1 + 3c_x + 2c_x^2)\frac{\Delta x^2}{6} \\ &\quad \left. + C_9\, \Delta y^2 \frac{c_y^2}{3} + C_{10}\, \Delta z^2 \frac{c_z^2}{3} \right], \end{aligned} \tag{19}$$

and for the diffusive one:

$$\begin{aligned} F^{(\mathrm{dif})}_{i-1/2,\,j,k} &= \frac{1}{Re}\frac{\Delta t}{|\Omega|} \int_{y-\Delta y/2}^{y+\Delta y/2} \mathrm{d}y' \int_{z-\Delta z/2}^{z+\Delta z/2} \mathrm{d}z' \mathbf{n} \cdot [E_t^{(3)} + R_s^{(2)}E_t^{(1)}] \underline{\nabla} v_j(x - \Delta x/2, y', z', t^n) \\ &= \frac{\Delta t}{\Delta x Re} \left[C_2 + C_5\, \Delta y \frac{c_y}{2} + C_6\, \Delta z \frac{c_z}{2} + C_8\, \Delta x(1 + c_x) \right], \end{aligned} \tag{20}$$

where $c_{x_j} = v_j\, \Delta t / \Delta x_j$ are the local Courant numbers and C_r are the polynomial coefficients, such that $v_j(\mathbf{x}, t) = \mathbf{C} \cdot \mathbf{P}^T$ with $\mathbf{P} = (1, x, \ldots, yz, \ldots, z^2)$. The coefficients C_r are determined depending on the local flow direction. Stability restrictions are determined by the functional relation between local Courant numbers and the cell Reynolds number (see Reference [9]).

For what is regarded as the projection step, the elliptic equation is discretized by the second-order central formula and solved by means of an iterative method.

For the 2D linear wave equation, this scheme formally leads to third-order-accuracy, as demonstrated in Reference [10]. Many test cases for 2D Navier–Stokes equations (lid driven cavity, natural convection, backward-facing step, etc.) at high Reynolds number can be found [9,10]. In order to assess the accuracy of the present method for 3D Navier–Stokes equations, it was applied to an analytical time-dependent benchmark [13]. The test was performed on grids ranging from five to ten cells for each co-ordinate, where the computational domain was a cube box of unity side. Figure 4 reports the velocity errors at $Re = 1$ and 100 against the mesh size in a double logarithmic scale. The error was computed in the L_2 norm, as in Reference [13]. As expected, at $Re = 100$ the accuracy order is lower, owing to non-linear terms relevance, but it is still ≈ 2. Even if this benchmark can not be indicative of real cases, it confirms the capability of the present scheme to be adopted at high cell Reynolds number. However, for highly non-linear cases, some improvements could be made by using a corrector step to better evaluate the advective terms in Equations (8) and (9).

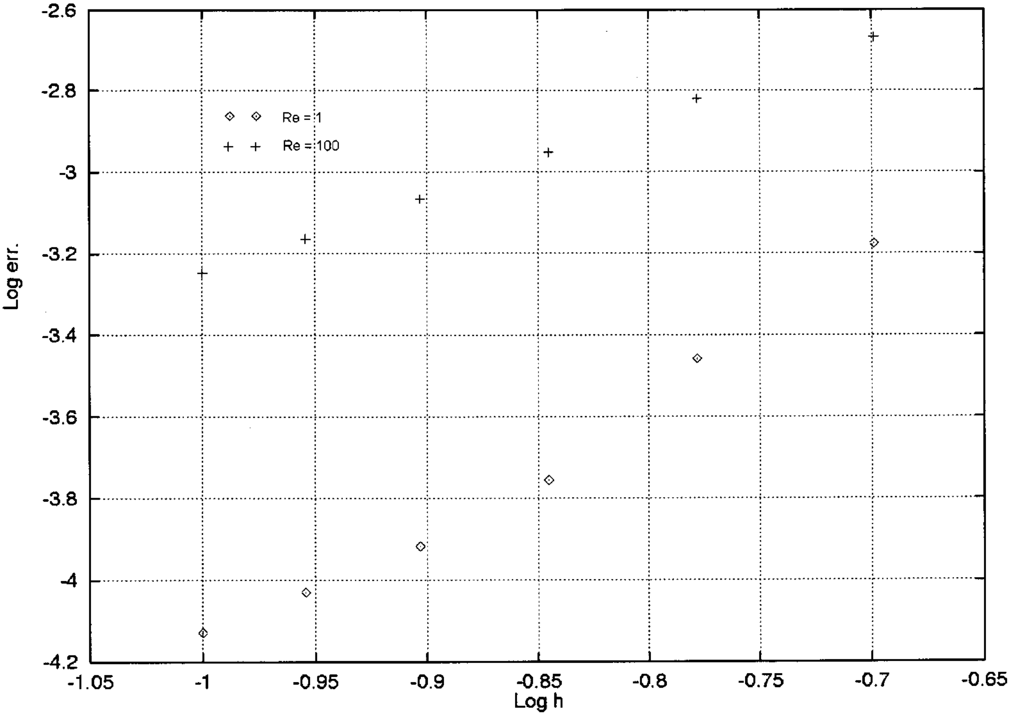

Figure 4. Benchmark for three-dimensional Navier–Stokes equations: resulting error in the L_2 norm versus mesh size h. Data are represented on double logarithmic scale for $Re = 1$ and 100.

4. RESULTS FOR LAMINAR REGIMES

In order to assess the present numerical method more deeply, we first performed some computations concerning laminar flows. In this section, owing to the fact that experimental data [8] are related to inflow conditions that can not be exactly reproduced in the numerical experiments, we tested the influence of two different inlet velocity profiles. It is well-known that the shape of the inflow velocity profile, as well as the presence of lateral walls, strongly affects the flow field. Unlike other authors [3,4], who used periodic or inviscid conditions, the present study adopted no-slip conditions in the spanwise direction, in order to better compare numerical results with the experimental ones. The first tested inflow was a fully developed 3D profile obtained by the solution of the Poisson equation on the (z, y)-plane:

$$\frac{\partial^2 u}{\partial z^2} + \frac{\partial^2 u}{\partial y^2} = Re\,\frac{\partial p}{\partial x} = \text{const}, \tag{21}$$

associated with homogeneous Dirichlet boundary conditions, i.e. the solution of the steady Navier–Stokes equations for parallel flows ($v = w = 0$). The field $u(0, y, z)$ is normalised with respect to the maximum velocity. The second inflow tested was obtained by repeating, along the spanwise direction, the 2D profile corresponding to the midplane section of the previous 3D inflow. More details are shown in Figure 5. In this way, both of these profiles maintain the same Reynolds number, but different flow rates are obtained. The choice of considering $\bar{U} = 2/3\,U_{\max}$, as reference velocity agrees with that of Armaly [8]. Moreover, an assessment of the scheme can be made to find if the numerical diffusion is not so high as to lead to the same solution, irrespective of different numerical inflow conditions.

In all cases presented in this section, the aspect ratio ($W/H = 18{:}1$) of Armaly [8] was used. The channel length is 20 times the step height in order to ensure a small influence of the outflow section, where vanishing normal second derivatives are imposed. The domain was discretized by a $60 \times 32 \times 120$ grid, having first performed a grid refinement to ensure that such a grid point number was sufficient to obtain a grid independent solution.

The computational time was ≈ 60 h for each run on a HP workstation equipped with PA-8000 RISC processor (160 Mflps). The goal of these computations was to show the variation of the reattachment length for a Reynolds number ranging up to 800, which probably represents the threshold to ensure an asymptotic steady flow [5]. The reattachment length at the midsection, normalised by the step height, is shown in Figure 6 to be in good agreement with the experimental one for both inflow conditions, up to $Re \cong 500$. This value is the limit where 2D assumptions can be considered valid [8]. It appears that for $500 < Re < 800$, the

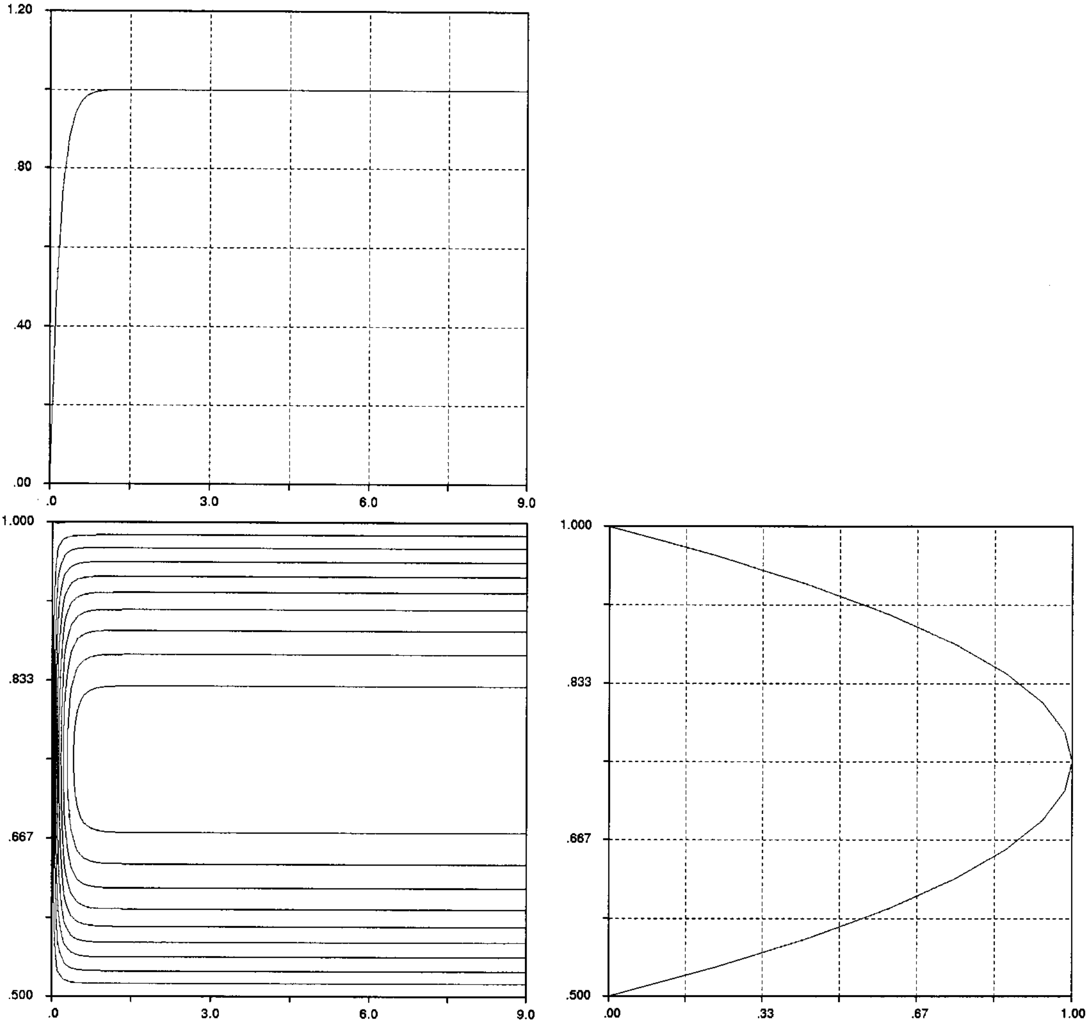

Figure 5. Contour pattern of the 3D inlet velocity profile $u(0, y, z)$. Length scales are altered for plotting purposes. The section profile at $y/H = 0.5$ is shown at the top, and the section profile at $z/H = 9$ is on the right. The latter, repeated along the spanwise direction, is the profile adopted for the 2D inflow.

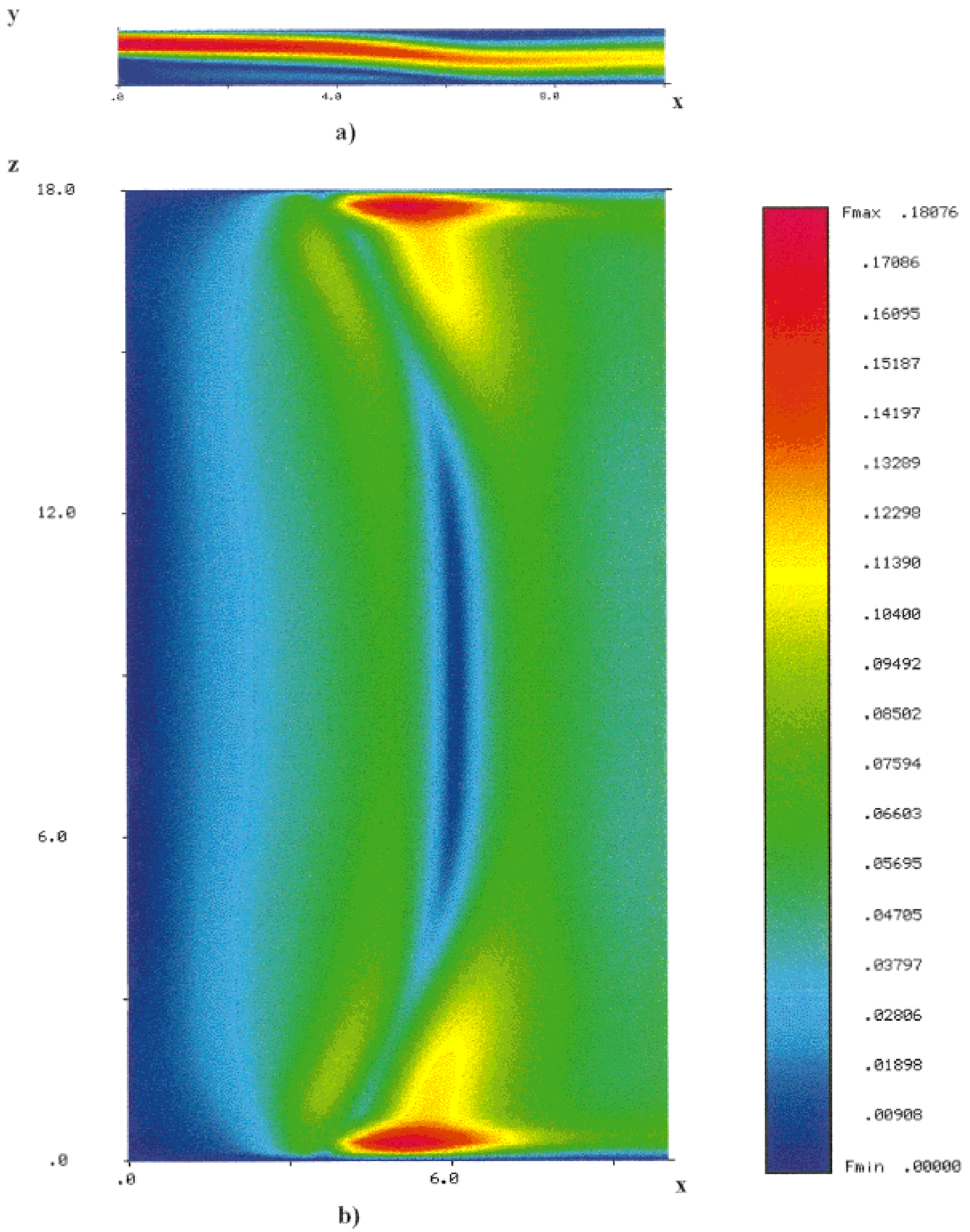

Plate 1. Shaded map of the velocity amplitude field for 2D inlet at $Re = 700$; (a) (x, y)-plane at $z/H = 9$; (b) (x, z)-plane near to the bottom wall. Velocity values are non-dimensionalized by $1.5\bar{U}$. Values in the colour map refer only to (b).

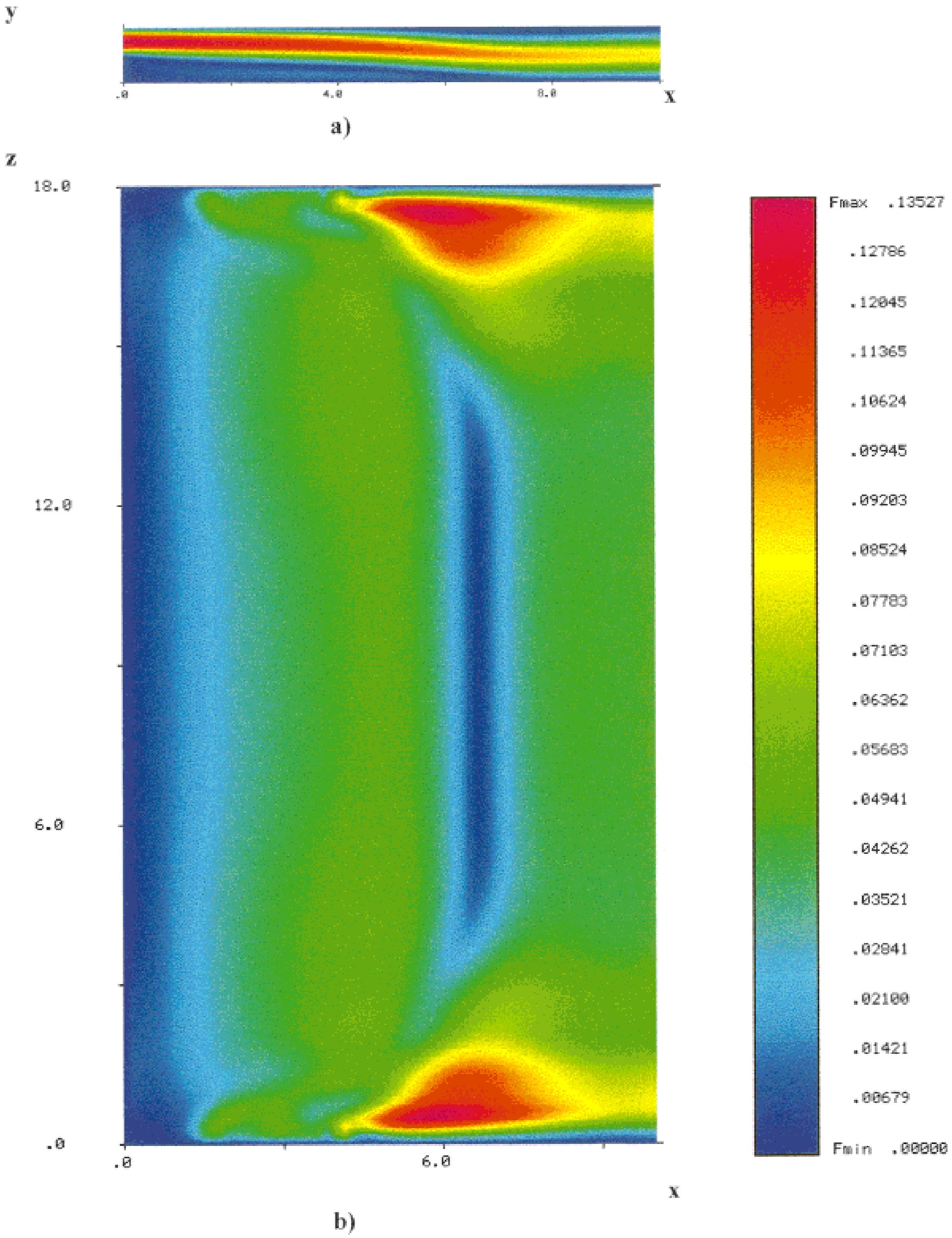

Plate 2. Shaded map of the velocity amplitude field for 3D inlet at $Re = 700$; (a) (x, y)-plane at $z/H = 9$; (b) (x, z)-plane near to the bottom wall. Velocity values are non-dimensionalized by $1.5\bar{U}$. Values in the colour map refer only to (b).

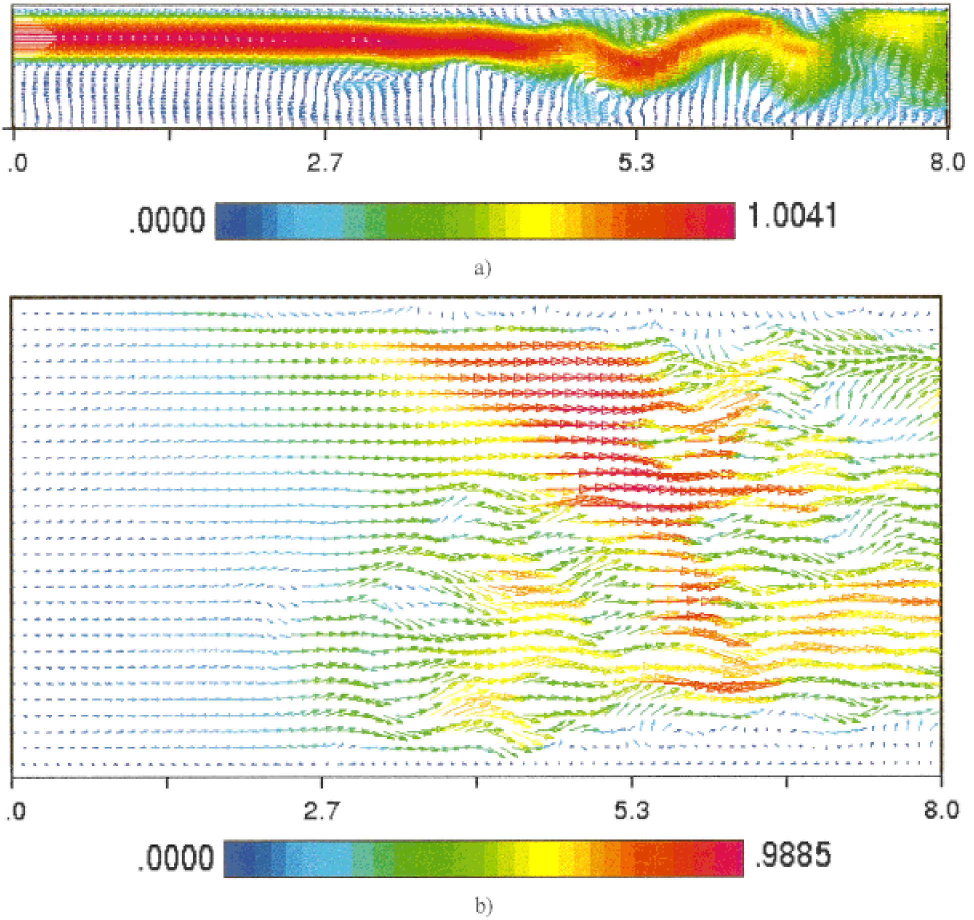

Plate 3. Instantaneous velocity vector plot at $Re = 6600$ in the: (a) (x, y)-plane at $z/H = 2$ and (b) (x, z)-plane at $y/H = 0.5$ The representation is limited to $x/H = 8$.

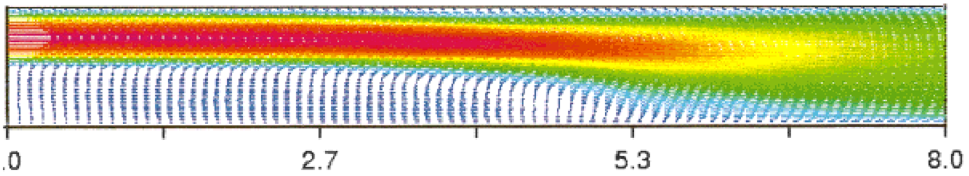

Plate 4. Average velocity vector plot at $Re = 6600$ in the: (x, y)-plane at $z/H = 2$. The representation is limited to $x/H = 8$.

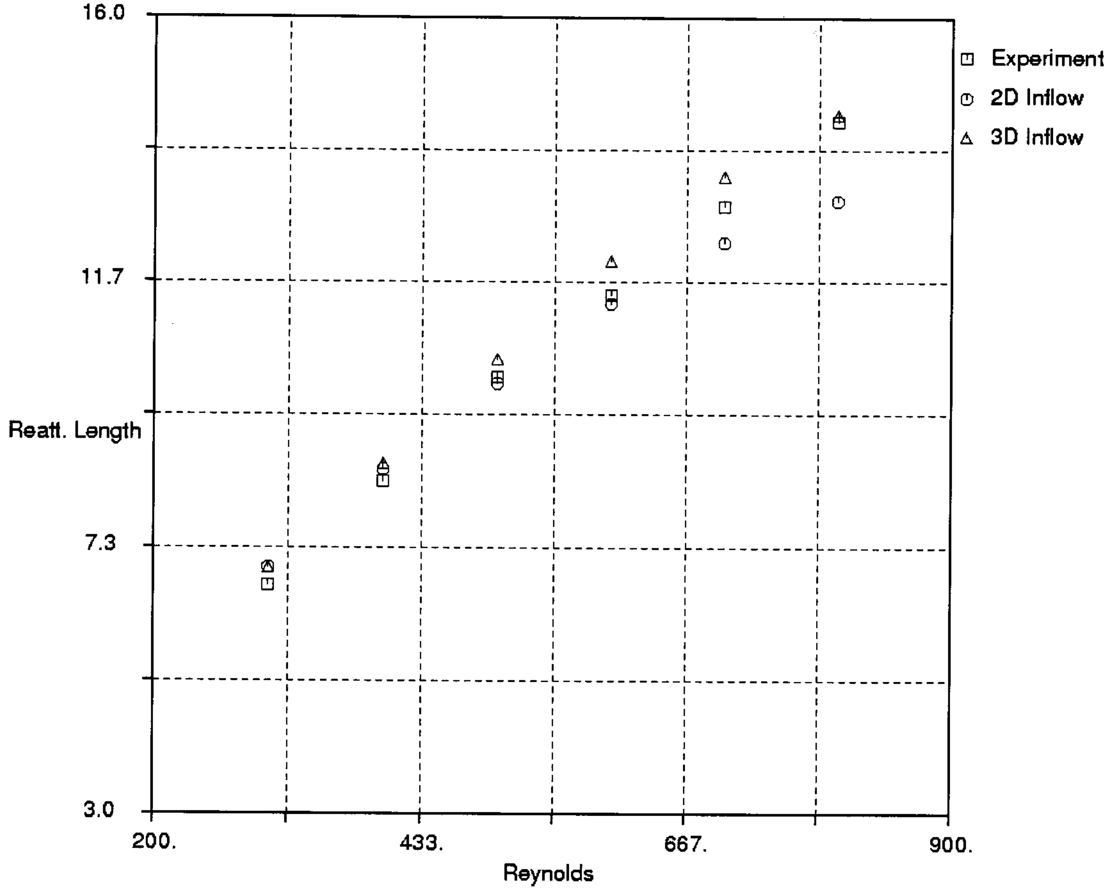

Figure 6. Normalised reattachment length x_r/S versus the Reynolds number in laminar regime, as computed with 2D and 3D inflow conditions.

reattachment length assumes a different behaviour, depending on the inlet profile. In particular, the 3D inflow generates values slightly greater than the experimental one, whilst the 2D inflow drives to lower ones. Three-dimensional simulation with 2D inlet basically provided the same values of the reattachment length compared with those obtained by a 2D simulation, which are not reported here for sake of brevity. When the 2D simulations were made the channel upstream of the step was also considered and it was assessed that, for laminar flow, the velocity profile at the step edge does not depend on the downstream field. Based on this observation, 3D simulations were made without the channel upstream of the step.

The behaviour of the reattachment length, shown in Figure 6, can be explained by comparing the resulting flow fields as shown in Plates 1 and 2. For 2D inflow conditions, at $Re = 700$, the velocity amplitude patterns at midplane section (a) and close to the bottom wall (b) are shown in Plate 1. The fields corresponding to the case with 3D inflow are shown in Plate 2. As clearly shown in Plate 2(b), the 3D effects are responsible for a generation of stronger spanwise velocity components that force the flow to stay attached along the upper wall for a longer distance, by increasing the primary reattachment length (see Plate 2(a)). This situation is clearer in Figure 7, where the vector plots at $x/H = 6.6$ are shown for both inflow conditions in a region of the (z, y)-plane ranging from $z/H = 0$ to 5.1. Finally, the computation at $Re = 800$ did not lead to a fully steady solution, as the velocity components, close to the outflow region, were slowly oscillating.

In order to better understand the three-dimensional structure of the flow field, both in steady and unsteady regimes, a suitable investigation tool has been built. Focusing our attention on the vorticity field, we reconstructed the main vortex tubes by directly applying the definition.

5. A DESCRIPTION OF THE VORTICITY FIELD BASED ON VORTEX TUBES RECONSTRUCTION

The analysis of the vorticity field can help to understand many features of BFS flow. Owing to the three-dimensional character of the flow, the physical picture coming from the numerical calculations of the velocity field can be completed by building the integral lines of the vorticity field.

Note that, in primitive variable formulations, the vorticity represents an auxiliary variable that can be obtained by a suitable interpolation of the discrete velocity field. At present, a linear interpolation for each direction is performed, in order to obtain the velocity gradient field in the domain D. For laminar regimes this is expected to be a sufficiently accurate approximation.

Starting from a finite number of points distributed in a uniform way along a certain initial curve, the integral lines of the vorticity field $\boldsymbol{\omega}$ through each point are numerically built. The integration is terminated when either the initial point or the boundary is reached.

An open question regards the choice of the generator curve. At least for flow fields that are 'mirror-like' with respect to the spanwise midsection (i.e. the velocity components parallel and normal to this plane are symmetric and anti-symmetric, respectively) a possible simple choice seems to place this curve on the symmetry plane, corresponding to an iso-line of the spanwise vorticity field ω_z, being ω_x, $\omega_y \cong 0$ in a neighbourhood of this section.

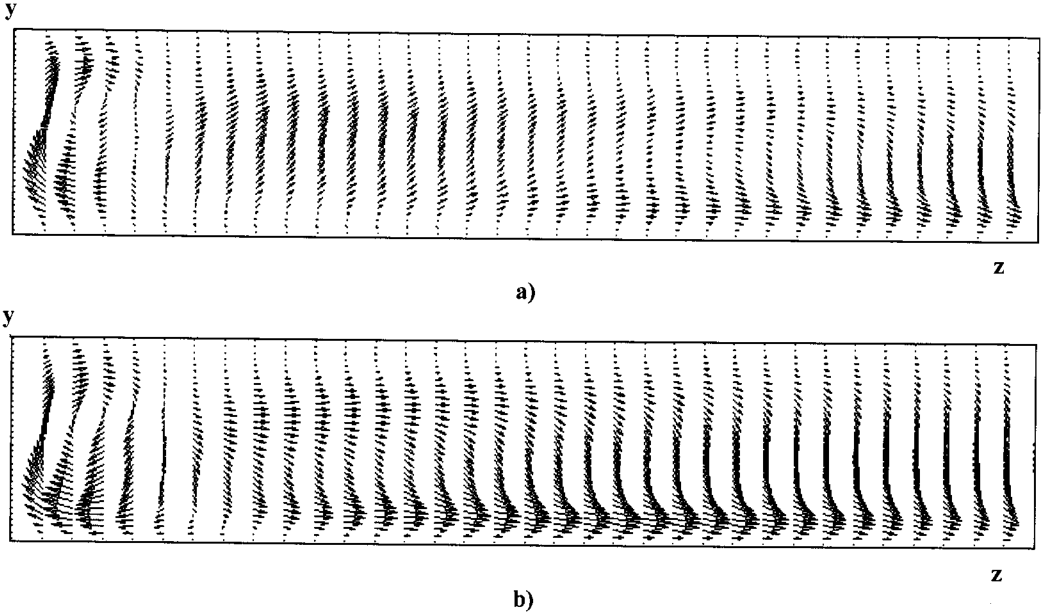

Figure 7. Velocity vector plot in the (z, y)-plane at $x/H = 6.6$ for z/H ranging from 0 to 5.1. (a) 2D case; (b) 3D case.

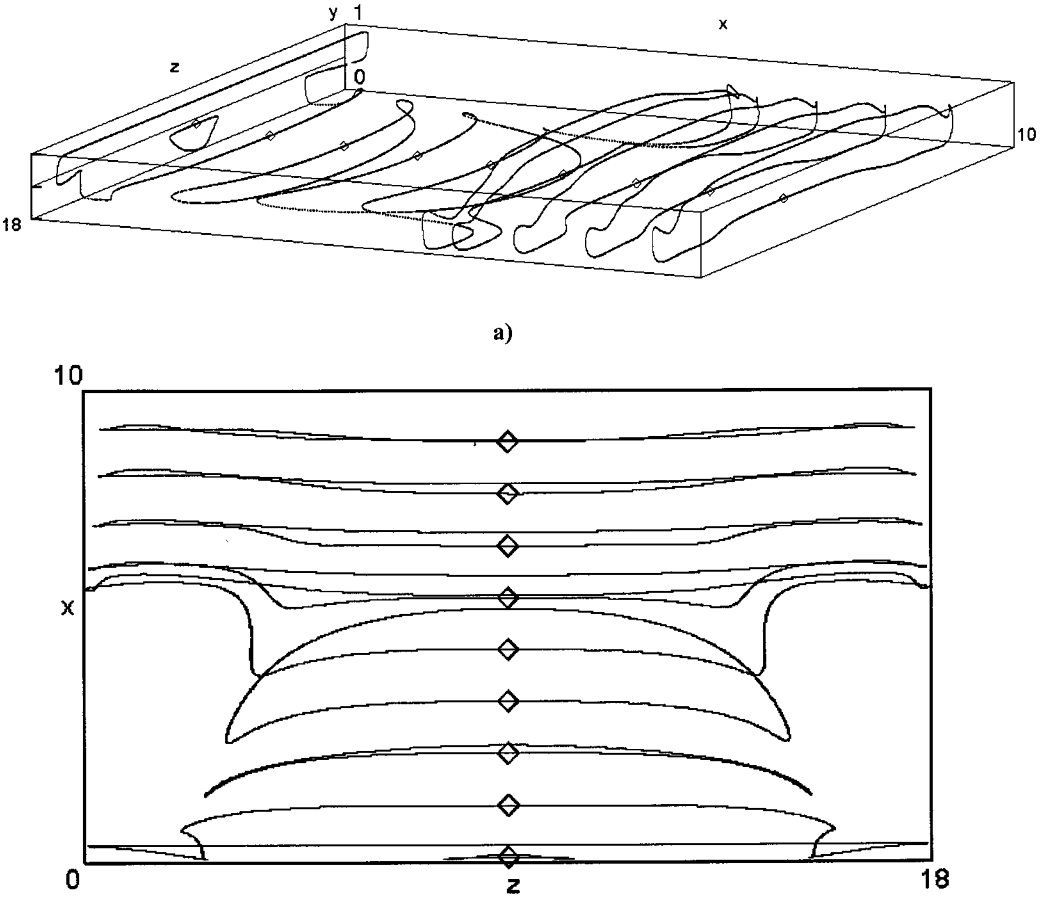

a)

b)

Figure 8. Vortex lines reconstruction starting from an iso-vorticity line at $\omega_z = -2.1\bar{U}/H$ for steady flow at $Re = 700$ and 3D inlet: (a) perspective view; (b) top view.

As an example of the reconstruction procedure, corresponding to the steady solution at $Re = 700$, for a channel with $W/H = 18$ and $L/H = 10$, the structure obtained starting from the iso-line at $\omega_z = -2.1\bar{U}/H$ is shown in Figure 8. Both the perspective (a) and top (b) view are presented. The initial positions are represented by markers and the spanwise length scale (a) is altered for plotting purposes.

The structure of the vorticity field appears to be quite complex: it exhibits a strong three-dimensional character, as can be seen particularly from the top view. Two different zones can be recognised: the lower one enclosing part of the primary recirculating region, just behind the step, and a Poiseuille-like structure, downstream of the reattachment of the flow, the shape of which is strongly affected by three-dimensional effects due to the presence of lateral walls.

Such a reconstruction procedure can also be used to follow the motion of simple vortex tubes for short times, by building the tube with a suitable time step during its evolution. The initial generator curve is chosen as that corresponding to a given iso-vorticity line on the midplane. At later times, the generator line can be either that corresponding to its Lagrangian evolution (i.e. the image of the initial curve), or to the new iso-line at the same vorticity value.

For instance, the latter choice has been made to study the start-up phase of the flow, as will be discussed in the following. These two choices do not lead to the same result, due to diffusion and stretching effects[5].

In Figure 9, corresponding to the case of 3D inlet at $Re = 400$, $W/H = 2$ and $L/H = 6$, a time sequence (a–c) of the iso-vorticity lines at the values 0 and $-0.6\bar{U}/H$ is shown. The sequence shows the development of the disturbance due to the sudden expansion along the channel. The iso-line corresponding to the zero spanwise vorticity is considered as representative of the boundary of the main recirculation region. The size of this region grows in time to a final stationary value $x_r/S = 7.8$. The reconstruction procedure has been applied only to the marked branches of the iso-lines. The corresponding structures are shown in Figure 10. For sake of clarity, the structure through the upper branch of the iso-line in Figure 9(a) has not been built, with the shape of the resulting tube being completely known. With reference to the steady configuration (Figure 10(c)), the main reverse flow region can be easily recognised, with little elongating in the spanwise direction for this small aspect ratio and a flow region describing the transition towards the 'Poiseuille-like' flow, downstream of the reattachment.

The above reconstructed structures can not be interpreted as vortices in the common sense. Moreover, this criterion is ambiguous, with the resulting vortex tubes depending on the

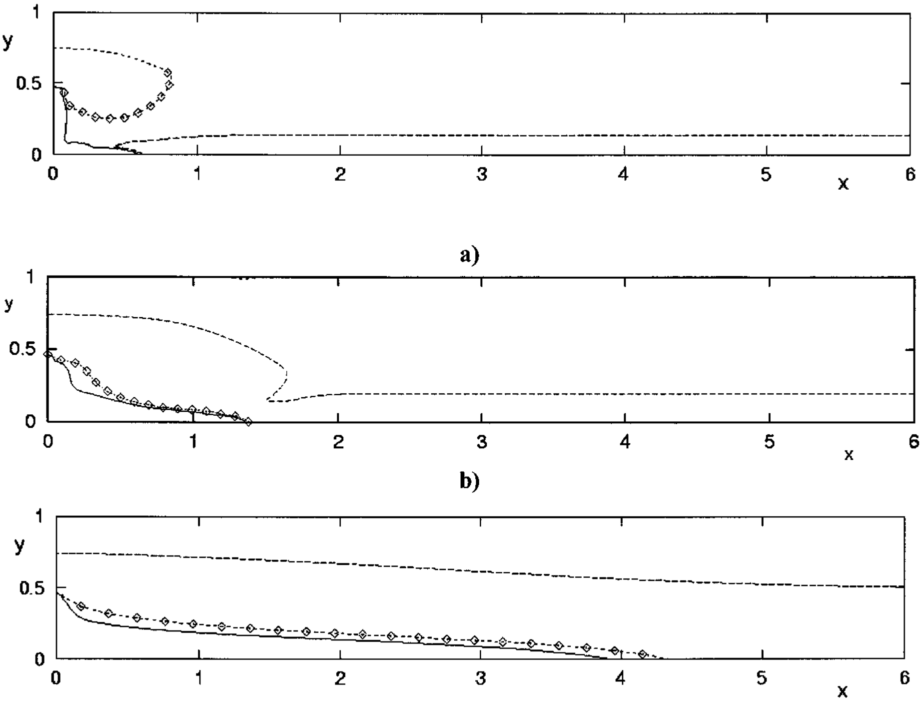

a)

b)

c)

Figure 9. Iso-vorticity lines $\omega_z = -0.6\bar{U}/H$ (dot lines), $\omega_z = 0$ (solid lines) at three different times; (a) $T = 0.85H/\bar{U}$; (b) $T = 2.09H/\bar{U}$; (c) $T = 38.97H/\bar{U}$. Markers represent the point distribution along the generator curves.

---

[5] Even when the generator curve is the image, at the different times of an initial given curve, the resulting structure does not correspond to the image of the initially reconstructed structure. On the other hand, if the initial structure were followed in a Lagrangian way, it would loose its basic property to be a vortex surface.

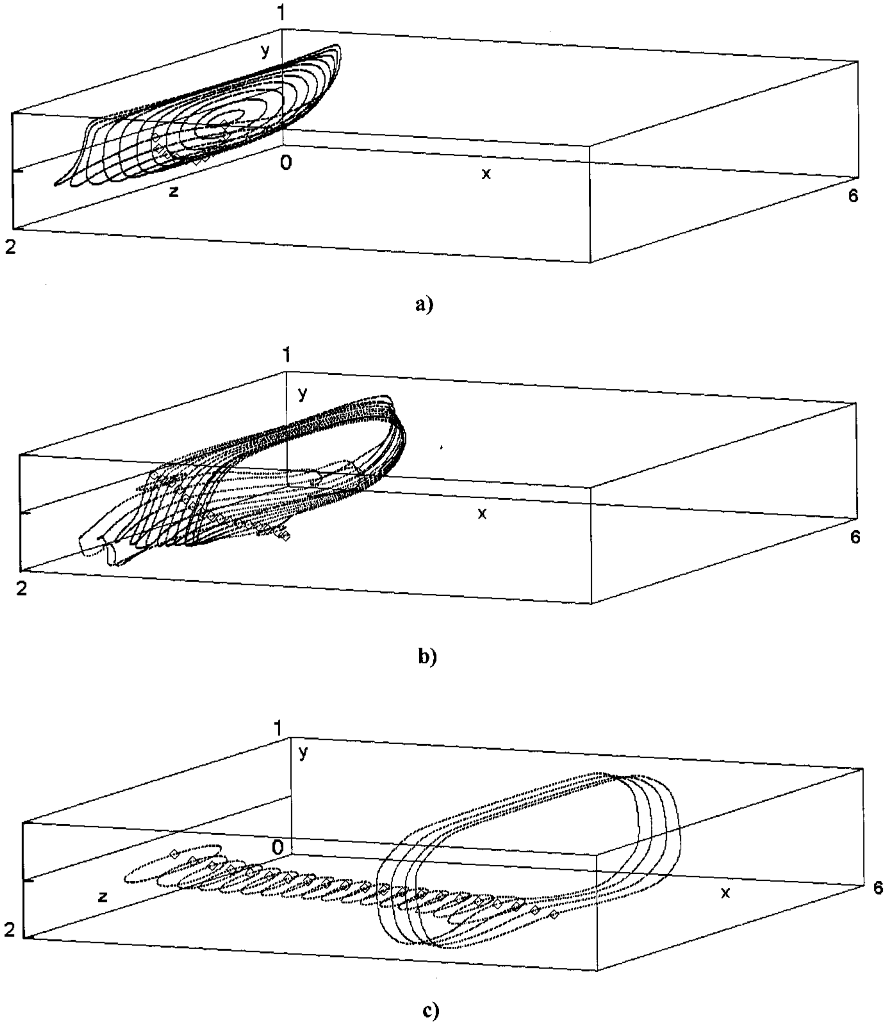

Figure 10. View of three-dimensional vortex lines at $Re = 400$ at three different times; (a) $T = 0.85H/\bar{U}$; (b) $T = 2.09H/\bar{U}$; (c) $T = 38.97H/\bar{U}$. Markers represent the initial positions along the generator curves (see also Figure 8).

subjective choice of the generator curve. On the other hand, by choosing an iso-line corresponding to a significant vorticity value, as the initial curve for the lines integration, the reconstructed structure is more meaningful than vorticity iso-surfaces.

6. A SURVEY OF VORTICES DETECTION CRITERIA

The reconstruction procedure presented in the previous section does not necessarily provide an identification of the coherent structures (i.e. vortices) which play an important role in the dynamics of separated flows. Vortices are commonly defined as regions of concentrated vorticity, having a lifetime much longer than their turnover time.

The development of techniques which can identify such structures has found that their definition cannot be based on the analysis of the velocity gradient field alone. In fact, many researchers have pointed out that the local behaviour of the pressure must be taken into account too. As shown in Reference [14], classical methods for vortices detection, based on the local pressure minimum or on the vorticity amplitude, are not recognised as being universally valid, depending on the type of flow which is under discussion. This lack of universal validity also affects the more recent criteria, based on the analysis of the velocity gradient invariants.

Three different criteria have been herein employed: (i) the criterion proposed by Chong *et al.* [15], according to which *a vortex core is a region of space where the velocity gradient tensor has complex eigenvalues*; (ii) that of Hunt *et al.* [16], according to which *a vortex is a region with both a positive second invariant (Q) of the velocity gradient and low pressure*, and (iii) that recently proposed by Jeong and Hussain [14], which summarises the essential features of the previous ones. According to the last criterion, a vortex core is defined as *a connected region with two negative eigenvalues of* $\mathbf{S}^2+\Omega^2$, where $\mathbf{S}$ and Ω are the symmetric and anti-symmetric part of $\nabla\mathbf{u}$, i.e. the rate of strain and the rate of rotation tensors, respectively. This criterion implicitly considers the influence of the local velocity gradient, as well as that of the local pressure and it is equivalent to require the second largest eigenvalue (λ_2) of $\mathbf{S}^2+\Omega^2$ to be negative.

In order to investigate the feasibility of the above criteria to detect vortices when applied to BFS flows, we first considered the flow field during the start-up phase at $Re=400$, already presented in the previous section.

For the spanwise midplane section, the application of (i) and (iii) provided almost exactly the same detected regions. This fact is due to the symmetry of the flow with respect to the midsection, that makes the velocity gradient have the form

$$\nabla\mathbf{u}\cong\begin{pmatrix} a & d & 0 \\ e & b & 0 \\ 0 & 0 & c \end{pmatrix}, \tag{22}$$

with $a+b+c=0$ from the incompressibility constraint. Then, in a neighbourhood of the midsection, the flow can be seen as locally two-dimensional, with out of plane strain.

The eigenvalues of $\mathbf{S}^2+\Omega^2$ are

$$\lambda_{1,2}=[a^2+b^2+2ed\mp|c|\sqrt{(a-b)^2+(e+d)^2}]/2; \quad \lambda_3=c^2. \tag{23}$$

For a sufficiently small value of $|c|$ (as it results in the case of 2D inlet or for a high aspect ratio), we approach the eigenvalues for a planar flow $\lambda_1=\lambda_2=a^2+ed$. In this case, definitions (i) and (iii) are equivalent, as well as the definition (ii), if the low pressure condition is disregarded.

Figure 11 shows, in terms of the negative λ_2-contour patterns, the zones identified by using the criterion (iii). During the transient phase (a–b), the detected regions represent the main vortical structures shedding from the step edge and the upper wall. This latter corresponds to a small recirculating region that hardly appears in Figure 9(b), because of the very low vorticity value chosen. On the other hand, for the steady field (c) the resulting picture is misleading; the downstream identified region does not correspond to an actual local concentration of vorticity. The same features were also observed for the steady field at $Re=700$ (not reported here). Such a misrepresentation is due to a little predominance of the rotation on the strain rate, as their intensities are not significant in steady regimes. Finally, by applying criterion (ii), that requires $Q=(\Omega_{ij}\Omega_{ij}-S_{ij}S_{ij})/2>0$, no vortex regions are detected until the pressure constraint is maintained.

In order to better investigate the issue, Figure 12 reports the scatter plot of $S_{ij}S_{ij} = \mathrm{trace}(\mathbf{S}^2)$ against $\Omega_{ij}\Omega_{ij} = -\mathrm{trace}(\Omega^2)$ for the steady flow at $Re = 700$. Herein the velocity gradient is non-dimensionalized by $U_{\max}/H$. For all represented grid nodes, data lie near a 45° line through the origin, i.e. rate of strain and rotation are of the same magnitude. At these moderate Reynolds numbers, each point appears to have a 'sheet-like' motion [17,18]. As a conclusion, the detection of vortices in such types of flow requires a more specific study, as the definition of vortex cores in terms of relative importance of rotation and strain rates is not satisfactory.

7. PERSPECTIVES AND CONCLUDING REMARKS

The present research is mainly intended as a preparation of some methodologies to analyse high Reynolds number flows, including CFD techniques and flow investigation tools. However, much work is still needed to assess the application of the present numerical scheme to turbulent flows, while the investigation of coherent structures results in a cumbersome topic. It is impossible to exhaustively face this double effort in the present paper, nevertheless it is worthwhile to address some guidelines.

The simulation of high Reynolds number flows presents several difficulties, owing to the appearance of a wide spectrum of characteristic length and time scales. Direct numerical simulation requires a great computational effort in order to accurately represent the finest scales (e.g. [19]). On the other hand, modelling the smallest scales, not resolvable on practical grids, represents an alternative approach (large eddy simulation) that decreases the computational effort but produces many other problems which are still under discussion. Some recent papers (e.g. [20,21]) have contributed to the clarification of how numerical analysis is strictly

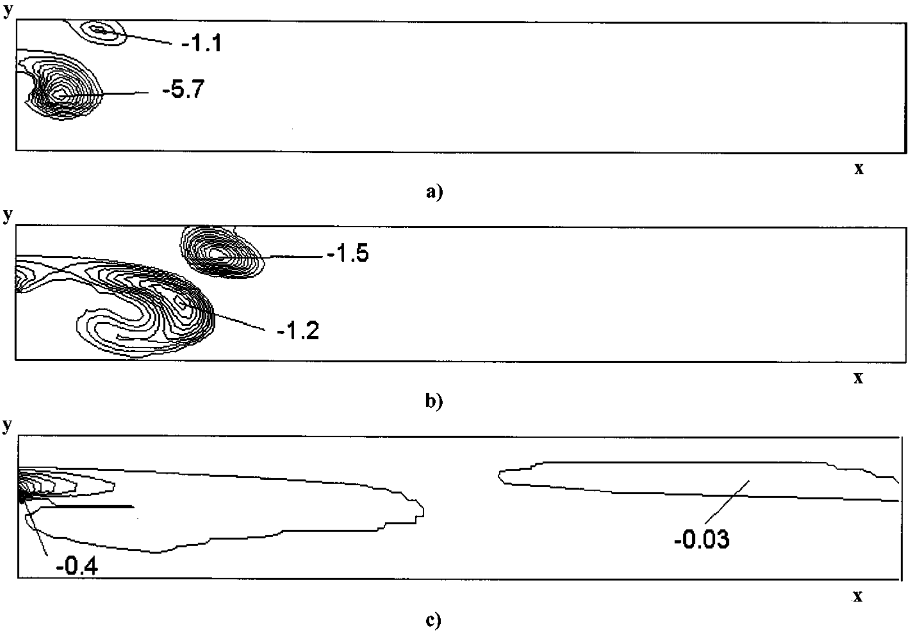

Figure 11. Iso-line patterns of $\lambda_2 < 0$ at $Re = 400$. The time instants correspond to those of Figures 8 and 9. The local minimum values are indicated.

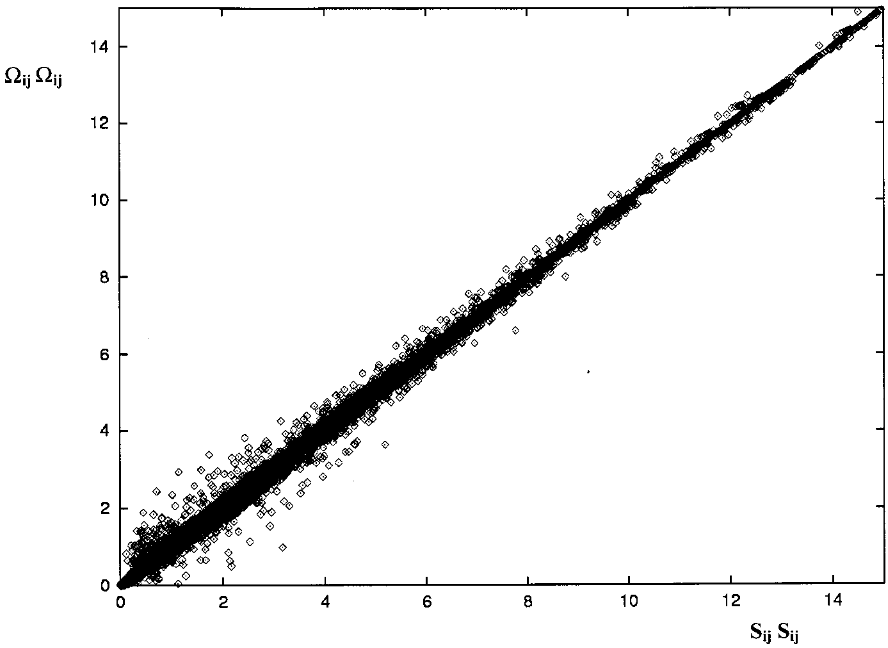

Figure 12. Scatter plot of the rotation versus strain rate for steady flow at $Re = 700$. Velocity gradient values are non-dimensionalized by $1.5\bar{U}/H$.

related to the development of subgrid scale (SGS) models, particularly because any model must be defined by means of a discrete equation that may strongly affect the final results.

At present, we have assessed the capability of the local average-based numerical procedure in simulating flows, up to incipient transitional regime, maintaining high the cell Reynolds number. For turbulent flows the present method, as it has been formulated, does not contain any explicit SGS model. Nevertheless, the local average acts as a box filter in the physical space and the reconstruction acts as a closure of the problem (as shown in Section 2), so that the present numerical method results are naturally linked with a large eddy simulation, as noted in References [10,22]. In particular, even if no SGS model is adopted, weak formulation and reconstruction operation allow the so-called Leonard terms to be taken into account implicitly (see Reference [22]). For this reason we expect large scales to be well represented.

In order to make some preliminary observations, a simulation of BFS flow at $Re = 6600$ has been performed into a channel with a non-dimensional length $L/H = 10$ and an aspect ratio $W/H = 4$, by adopting a $100 \times 52 \times 30$ grid. The code ran for a time interval sufficiently wide to obtain a steady statistic state[6]. A picture of the fully developed unsteady velocity vector field is reported in Plate 3, in the (x, y)-plane for $z/H = 2$ (a) and in the (x, z)-plane for $y/H = 0.5$ (b). For sake of completeness, a time average has been performed for an interval of 100 non-dimensional time units. The resulting average velocity vector field at the midsection is shown in Plate 4 and the reattachment length is $x_r/S = 11.4$, much greater than the experimental one [8], estimated in $x_r/S \approx 8$. This fact is mainly due to the lower spanwise aspect ratio adopted and to the imposed 3D conditions at the inlet.

---

[6] As an example of the computational effort, this run requires about 7 days on a workstation IBM RISC 6000 3B-T (40 Mflps) to reach a steady statistic condition.

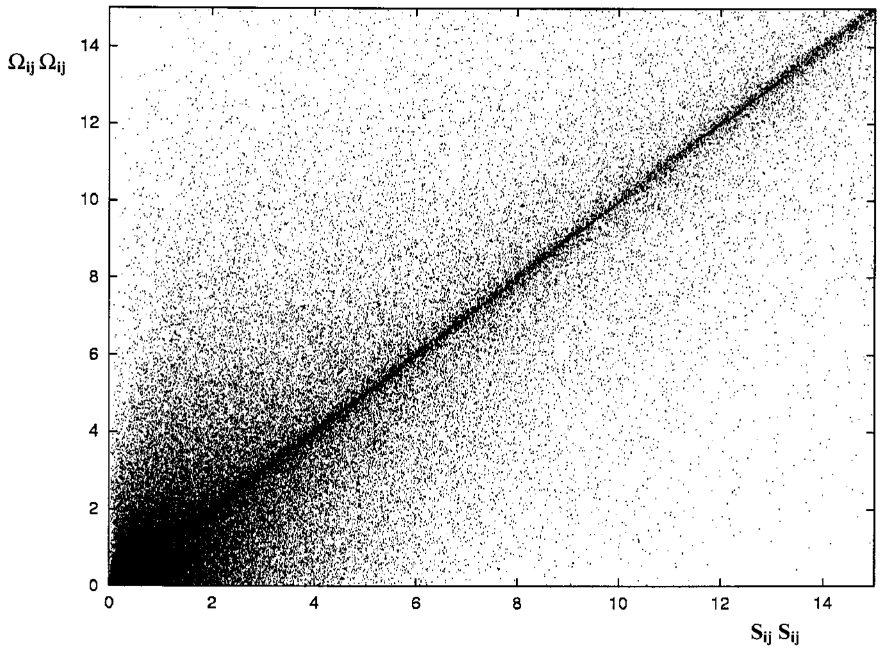

Figure 13. Scatter plot of the rotation versus strain rate for unsteady flow at $Re = 6600$. Velocity gradient values are non-dimensionalized by $1.5\bar{U}/H$.

For this case the analysis of the vorticity field is currently under development. In fact, when it is attempted to build vortex tubes from the instantaneous field, many difficulties should be overcome, as the appropriate choice of the generator curve (being absent any kind of symmetry in the flow, as it can be seen in Plate 3(b)) and the accurate reconstruction of the discrete velocity field. Moreover, strong three-dimensional effects, caused by the presence of lateral walls, make the reconstruction more complicated. Periodical boundary conditions could be imposed along the spanwise direction to by-pass this additional difficulty. The application of vortex detection criteria to BFS laminar flows already revealed some difficulties caused by the fact that rate of strain and rate of rotation generally are of the same order of magnitude. From the analysis of the scatter plot of $S_{ij}S_{ij}$ against $\Omega_{ij}\Omega_{ij}$ (Figure 13), it appears that a more complicated picture results for flow at $Re = 6600$, where, according to the discussed criteria, many regions can be identified as 'vortex cores'. Ranging the extent of such vortical regions over a wide interval of scales, a highly accurate interpolation of the discrete velocity field is required to compute the velocity gradient. A further step could result in a statistical analysis of the detected structures, by performing an ensemble average of the instantaneous λ_2-fields, as described in Reference [23].

Finally, the issues addressed in the introduction have been generally accomplished. Indeed, a numerical method for the simulation of three-dimensional incompressible flows has been developed and assessed. We also considered the influence of different inflow boundary conditions and some physical aspects of the flow were investigated by applying suitable tools for the investigation of the flow structure. This point has been addressed from two different points of view, which appear to be complementary. In fact, some differences appear by discussing the use of the vortex tubes reconstruction and the application of the vortex detection criteria. If we focus on the three-dimensional character of the flow, the vortex tube reconstruction appears to be a helpful approach which enables us to investigate the local behaviour of the vorticity field. On the other hand, the identification of significant vortical regions is needed when one investigates the dynamics of coherent structures, a matter in which it has been shown that other features of the flow, as well as vorticity, must be considered. The application of criteria for the vortex identification directly provides the space regions belonging to the vortex cores, during their evolution.

Work is in progress in order to explicitly compare the solutions of high Reynolds number flows obtained by means of the present method, with those presented by other authors based on different numerical procedures. A more suitable approach to detect vorticity structures is also needed.

REFERENCES

1. J. Kim and P. Moin, 'Applications of a fractional-step method to incompressible Navier–Stokes equations', *J. Comput. Phys.*, **59**, 308 (1985).
2. M. Ciofalo and M.W. Collins, 'k-ε predictions of heat transfer in turbulent recirculating flows using an improved wall treatment', *Numer. Heat Trans., Part B*, **15**, 21 (1989).
3. L. Kaiktsis, G.E. Karniadakis and Orszag, 'Onset of three-dimensionality, equilibria, and early transition in flow over a backward-facing step', *J. Fluid Mech.*, **231**, 501 (1991).
4. A. Silveira Neto, D. Grand, O. Metais and M. Lesieur, 'A numerical investigation of the coherent vortices in turbulence behind a backward facing step', *J. Fluid Mech.*, **256**, 1 (1993).
5. P.M. Gresho, D.K. Gartling, J.R. Torczynski, K.A. Cliffe, K.H. Winters, T.J. Garratt, A. Spence and J.W. Goodrich, 'Is the steady viscous incompressible two-dimensional flow over a backward-facing step at $Re = 800$ stable?', *Int. J. Numer. Methods Fluids*, **17**, 501 (1993).
6. K. Abe, T. Kondoh and Y. Nagano, 'A new turbulence model for predicting fluid flow and heat transfer in separating and reattaching flows-I. Flow field calculations', *Int. J. Heat Mass Trans.*, **37**, 139 (1994).
7. J.K. Eaton and J.P. Johnston, 'A review of research on subsonic turbulent flow reattachment', *AIAA J.*, **19**, 1083 (1981).
8. B.F. Armaly, F. Durst, J.C.F. Pereira and B. Schonung, 'Experimental and theoretical investigation of backward-facing step flow', *J. Fluid Mech.*, **127**, 473 (1983).
9. G. De Felice, F.M. Denaro and C. Meola, 'Multidimensional single step vector upwinded schemes for highly convective transport problems', *Numer. Heat Trans., Part B*, **23**, 425 (1993).
10. F.M. Denaro, 'Towards a new model-free simulation of high-Reynolds-flows: local average direct numerical simulation', *Int. J. Numer. Methods Fluids*, **23**, 125 (1996).
11. A.J. Chorin, 'Numerical solution of the Navier–Stokes equations', *J. Math. Comput.*, **22**, 745 (1968).
12. J.B. Bell, P. Colella and H.M. Glaz, 'A second-order projection method for the incompressible Navier–Stokes equations', *J. Comp. Phys.*, **85**, 257 (1989).
13. C. Ross Ethier and D.A. Steinman, 'Exact fully 3D Navier–Stokes solutions for benchmarking', *Int. J. Numer. Methods Fluids*, **19**, 369 (1994).
14. J. Jeong and F. Hussain, 'On the identification of a vortex', *J. Fluid Mech.*, **285**, 69 (1995).
15. M.S. Chong, A.E. Perry and B.J. Cantwell, 'A general classification of three-dimensional flow fields', *Phys. Fluids A*, **2**, 745 (1990).
16. J.C.R. Hunt, A.A. Wray and P. Moin, 'Eddies, stream, and convergence zones in turbulent flows', Center for Turbulence Research, *Report CTR-S88*, p. 193.
17. J. Soria, R. Sondergaard, B.J. Cantwell, M.S. Chong and A.E. Perry, 'A study of the fine-scale motions of incompressible time-developing mixing layers', *Phys. Fluids*, **6**, 871 (1994).
18. H.M. Blackburn, N.M. Mansour and B.J. Cantwell, 'Topology of fine-scale motions in turbulent channel flow', *J. Fluid Mech.*, **310**, 269 (1996).
19. H. Le, P. Moin and J. Kim, 'Direct numerical simulation of turbulent flow over a backward-facing step', *J. Fluid Mech.*, **330**, 348 (1997).
20. S. Ghosal and P. Moin, 'The basic equations for the large eddy simulation of turbulent flows in complex geometry', *J. Comput. Phys.*, **118**, 24 (1995).
21. S. Ghosal, 'An analysis of numerical errors in large-eddy simulations of turbulence', *J. Comput. Phys.*, **125**, 187 (1996).
22. F.M. Denaro, G. De Stefano and G. Riccardi, 'Local-average based numerical simulation of turbulent flows', *1st AFOSR Int. Conf. DNS and LES*, Louisiana Tech University, Ruston, Louisiana, USA, 1997, p. 273.
23. J. Jeong, F. Hussain, W. Schoppa and J. Kim, 'Coherent structures near the wall in a turbulent channel flow', *J. Fluid Mech.*, **332**, 185 (1997).